ADVANCED ENERGY MATERIALS
www.advenergymat.de

Uncovering the Electron-Phonon Interplay and Dynamical Energy-Dissipation Mechanisms of Hot Carriers in Hybrid Lead Halide Perovskites

*Christopher C. S. Chan, Kezhou Fan, Han Wang, Zhanfeng Huang, Dino Novko, Keyou Yan, Jianbin Xu, Wallace C. H. Choy, Ivor Lončarić, and Kam Sing Wong**

The discovery of slow hot carrier cooling in hybrid organic–inorganic lead halide perovskites (HOIPs) has provided exciting prospects for efficient solar cells that can overcome the Shockley–Queisser limit. Questions still loom over how electron-phonon interactions differ from traditional polar semiconductors. Herein, the electron-phonon coupling (EPC) strength of common perovskite films ($MAPbBr_3$, $MAPbI_3$, $CsPbI_3$, and $FAPbBr_3$) is obtained using transient absorption spectroscopy by analyzing the hot carrier cooling thermodynamics via a simplified two-temperature model. Density function theory calculations are numerically performed at relevant electron-temperatures to confirm experiments. Further, the variation of carrier-temperature over a large range of carrier-densities in HOIPs is analyzed, and an "S-shaped" dependence of the initial carrier-temperature to carrier-density is reported. The phenomenon is attributed to the dominance of the large polaron screening and the destabilization effect which causes an increasing-decreasing fluctuation in temperature at low excitation powers; and a hot-phonon bottleneck which effectively increases the carrier temperature at higher carrier-densities. The turning point in the relationship is indicative of the critical Mott density related to the nonmetal-metal transition. The EPC analysis provides a novel perspective to quantify the energy transfer in HOIPs, electron-lattice subsystem, and the complicated screening-bottleneck interplay is comprehensively described, resolving the existing experimental contradictions.

1. Introduction

Hybrid organic–inorganic lead halide perovskites (HOIPs) have been the center of attention in solar photovoltaic and light emitting materials research over the best part of last decade.[1–4] Their outstanding optoelectronic properties such as low defects, long balanced carrier diffusion length and large absorption coefficients have resulted in power conversion efficiencies in solar cells that rival traditional semiconductors.[5] The Coulombic interaction between the polar perovskite lattice and charge carriers can provide effective shielding from recombination and hence unwanted losses. Together with the ability to alloy with other halides, perovskites' band-edge can be tuned, leading to versatile applications in light emission, lasers,[6] and even quantum electronics.[7] An interesting aspect of HOIPs that has been commanding substantial research interest is the slow hot carrier (HC) cooling phenomenon. Charge carriers created by photons with photon-energy above the bandgap possess high energy that is lost as the carriers

Dr. C. C. S. Chan, K. Fan, Prof. K. S. Wong
Department of Physics and William Mong Institute of Nano Science and Technology
The Hong Kong University of Science and Technology
Clearwater Bay, Hong Kong, P. R. China
E-mail: phkswong@ust.hk

K. Fan
School of Physics
Sun Yat-sen University
No.135 Xingangxi Road, Guangzhou, Guangdong 510275, P. R. China

The ORCID identification number(s) for the author(s) of this article can be found under https://doi.org/10.1002/aenm.202003071.

© 2021 The Authors. Advanced Energy Materials published by Wiley-VCH GmbH. This is an open access article under the terms of the Creative Commons Attribution-NonCommercial License, which permits use, distribution and reproduction in any medium, provided the original work is properly cited and is not used for commercial purposes.
The copyright line for this article was changed on 9 March 2021 after original online publication.

DOI: 10.1002/aenm.202003071

Dr. H. Wang, Prof. K. Yan, Prof. J. Xu
Department of Electronic Engineering and Department of Chemistry
The Chinese University of Hong Kong
Shatin, New Territories, Hong Kong, P. R. China

Dr. Z. Huang, Prof. W. C. H. Choy
Department of Electrical and Electronic Engineering
The University of Hong Kong
Pokfulam Road, Hong Kong, P. R. China

Dr. D. Novko
Institute of Physics
Zagreb 10000, Croatia

Dr. I. Lončarić
Division of Theoretical Physics
Ruđer Bošković Institute
Zagreb 10000, Croatia

cool down to the band edge. This cooling is a major source of loss in solar cells, and fundamentally limits its power conversion efficiency. Excited carriers in traditional semiconductors cool down to the lattice temperature through phonon interactions in ultrafast time scales which make it practically impossible to extract them through electrodes. In HOIPs, it has been reported that the cooling rate of HCs is substantially lower than that of many solar cell materials, and around three orders of magnitude lower than GaAs for comparison.[8] This phenomenon in HOIPs opens up the possibility to realize ultra-efficient photovoltaics,[9] toward breaking the Shockley–Queisser limit.[10]

Immediately following photon absorption, charge carriers generated at energy positions in excess of the bandgap, will quickly redistribute through carrier–carrier scattering to occupy states described by Fermi-Dirac statistics.[11] These HCs gradually undergo energy relaxation through phonon interactions redistributing to the band edge. It has been widely accepted in HOIPs that the energies of the longitudinal optical (LO) phonon, that charge carriers strongly couple to through the Fröhlich interactions, are relatively low. In addition, the efficient Klemens channel for LO phonon decay, is shown by Fu et al., to be largely suppressed due to a large phonon bandgap.[12] The dominant carrier cooling mechanism at room temperature is the Fröhlich interaction occurring through the zone-center non-equilibrium LO phonon emission. A large LO phonon population is thus present, and as the carrier density rises above $\approx 10^{18}$ cm^{-3} the inefficient Klemens channel, responsible for LO phonon decay, results in a hot-phonon bottleneck effect. The cooling process is therefore slowed down, and as carrier density increases to larger than 10^{19} cm^{-3} multi-body effects start to dominate. At such high carrier densities, a reheating is induced by inter-band Auger recombination further prolonging the HC cooling.[13] Sum et al., first disclosed the interplay between hot-phonon bottleneck and Auger reheating effects at high carrier density in $MAPbBr_3$ bulk films and nanocrystals (NCs).[14] Accordingly, hot-phonon bottleneck effect can reduce the cooling rate during the first ≈2 ps, while the cooling process is even prolonged to tens of picoseconds due to inter-band Auger reheating. In addition, Yang et al. also reported that the phonon bottleneck effect induced by the acoustic-optical phonon up-conversion in $FAPbI_3$ bulk film can generate approximately ten times longer LO-phonon emission lifetime compared to its all-inorganic counterparts even at moderate carrier densities ($\approx 5 \times 10^{18}$ cm^{-3}).[15] Notably, one needs to pay extra attention to the distinction between the concept of "hot-phonon bottleneck effect" and "phonon bottleneck effect" when investigating the cooling mechanisms in HOIPs (see Note S1 in the Supporting Information for details).

Contrary to the hot-phonon bottleneck phenomena, HC cooling was shown to also slow down even at lower carrier densities beyond the threshold for hot-phonon bottleneck to occur.[16] It was found that in $MAPbBr_3$ the carrier cooling is slower than that in $FAPbBr_3$, and $FAPbBr_3$ is slower than the inorganic $CsPbBr_3$. The major disparity is thought to arise from the reorientation motion of the dipolar molecule in $MAPbBr_3$ and $FAPbBr_3$ that results in a faster rate of polaron formation compared to the all-inorganic $CsPbBr_3$ observed through optical Kerr effect spectroscopy.[17] Polarons were found to form quickly (0.3 ps) in the MA-perovskite compared to a Cs-perovskite (0.7 ps),[18] correlated to the slower rate of HC cooling in the hybrid perovskites.[17,19] The argument is that the large polarons can effectively protect the charge carriers, screening the Coulombic interaction that is responsible for scattering with LO phonons and effectively slowing down the carrier cooling. Furthermore, the organic cation can support a higher number of optical phonon modes which influence the respective perovskite's specific heat capacity, leading to the observation that inorganic perovskites exhibit a larger dependence of cooling rate with carrier density.[20]

Although the large polaron formation was shown to slow down HC cooling, this effective "shield" can break down at higher polaron densities. Since large polarons spread over multiple unit cells, when carrier density is high enough, the polarons begin interact and lead to destabilization. Niesser et al. reported this destabilization by showing a decrease in electronic temperature with increasing density at low excitation densities.[16] This opposes the trend of the hot-phonon bottleneck effect, in which the HC energy and excitation density increases simultaneously.[8,21] The observation was further discussed by Frost et al., who suggested a density at which polarons overlap and to the extent that the above-bandgap thermal energy is shared between the sea of polarons to be in the 10^{18} cm^{-3} region.[22] The change in the state of the HCs is described by the phenomenological Mott density, but to date, there are few reports that observe such changes if any to the cooling dynamics of HOIPs. In addition to the aforementioned effects, alternative relaxation channels due to atomic fluctuations, surface effects,[23] and intra-band Auger-type energy transfer can accelerate the carrier cooling process investigated extensively in quantum dot systems.[14] Though the time scale of the cooling dynamics can be quantified by the HCs cooling time and LO phonon lifetime,[9] the energy transfer in the electron-lattice subsystem, which combines both the cooling rate and temperature of HCs, cannot be reflected.

In this paper, HC cooling dynamics is investigated using transient absorption spectroscopy pumped at a fixed energy above bandgap and varied with pump fluences by ≈2 orders of magnitude. We introduce the electron-phonon coupling (EPC) coefficient (G_{el}) as a means to characterize the energy transfer from the energetic carriers to the lattice over a broad range of carrier densities. A simplified two-temperature model (TTM) is developed in attempt to quantify the G_{el} from HC relaxation following a monochromatic excitation. Importantly, we find that first the value of G_{el} in HOIPs is seen to differ with different organic cations. Second, that G_{el} remains consistent and fluctuates within error for a broad range of investigated carrier densities. The G_{el} coefficient provides a thermodynamic quantification of the energy transfer rate in the electron-lattice subsystems and provides a novel perspective to investigate the attenuated cooling phenomenon in HOIPs. Furthermore, an "S" shaped dependence of the carrier temperature with carrier density is presented, which we interpret as the competition between large polaron screening and hot-phonon bottleneck. Our analysis reveals the critical Mott density that distinguishes the dominant cooling phenomenon. To generalize the finding, we conduct the analysis on $MAPbBr_3$, $MAPbI_3$, $FAPbBr_3$, and $Cs_{0.05}(FA_{0.85}MA_{0.15})_{0.95}Pb(I_{0.85}Br_{0.15})_3$ films, all showing the same trends. Interestingly, the critical Mott density in MA-based sample is found to be larger than that in the FA-based

© 2021 The Authors. Advanced Energy Materials published by Wiley-VCH GmbH

and mixed-cation perovskites, resulting in smaller extracted Bohr radii in the first sort of materials. We subsequently use this technique to estimate the Bohr radii in novel mixed-cation perovskite, and present the exciton binding energy estimation as a comparison. Most importantly, our explication of the complicated interplay between large polaron screening and hot-phonon bottleneck effects helps to shed light on the hot-carrier harvesting in ultra-high-efficiency solar cell application.

2. Results

2.1. Extraction of Hot-Carrier Temperature from TA Spectra

Neat perovskite films $MAPbBr_3$, $MAPbI_3$, $FAPbBr_3$ of thickness 60 nm and $Cs_{0.05}(FA_{0.85}MA_{0.15})_{0.95}Pb(I_{0.85}Br_{0.15})_3$ of thickness 480 nm were prepared on transparent substrates (see Experimental Section for details). The absorption, as well as the photoluminescence (PL) spectra shown in Figure S1 (Supporting Information) clearly shows absorption onset and band edge emission for each film. Atomic force microscope (AFM) was used to verify the thickness and characterize the morphology of the first three samples (see Figure S2 in the Supporting Information). To study the HC cooling dynamics, TA spectroscopy was conducted at room temperature on the samples using a femtosecond broadband pump-probe technique. Spin-orbit coupling in perovskites split the conduction band into upper and lower optically accessible levels. In $MAPbI_3$, the bandgap is situated at ≈1.6 eV with a second transition at ≈2.5 eV.[24] We intend to generate hot carriers in the first conduction band only to avoid complications. A pump photon energy of 0.5 eV above the respective bandgap is used to keep a consistent excess energy of generated HCs. For example, ≈2.1 eV is used to excite in $MAPbI_3$.[22] **Figure 1**a shows the pseudo-color TA plot of $MAPbBr_3$ film excited with a calculated carrier density n_0 of 5.0×10^{18} cm^{-3} (estimated by method in Note S2 in the Supporting Information) at ≈2.9 eV, ≈0.5 eV above the bandgap of 2.39 eV.[24] A large positive signal due to the photo bleaching (PB) between 2.3–2.4 eV is present, indicative of carriers populating the band-edge. Initially the pump photons generate a broad PB signal that gradually narrows asymmetrically. The high-energy side of the signal relaxes leaving a long-lived PB at the ≈2.35 eV. A small redshift of the PB peak is observed from ≈2.35 eV at 0.1 ps to ≈2.33 eV. This is attributed to the energy- and

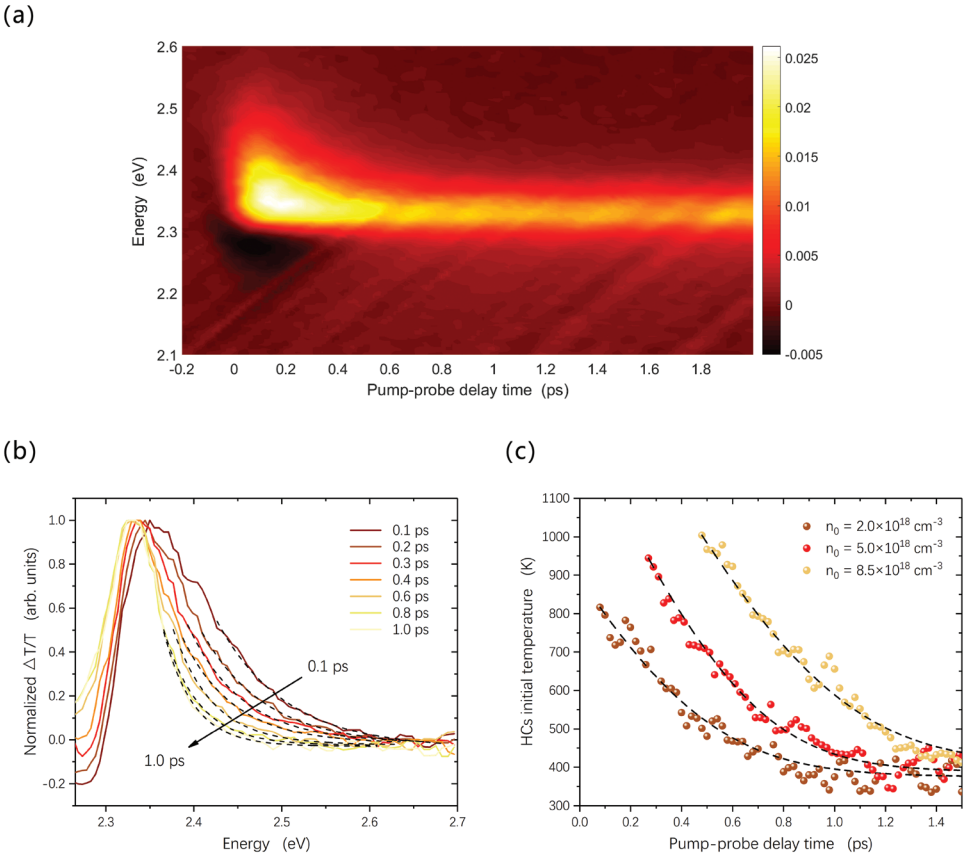

Figure 1. TA plot and cooling dynamics in the $MAPbBr_3$ sample. a) Pseudo-color TA plot which is excited at 2.89 eV, ≈0.5 eV above the bandgap. The sample is pumped at 50 μW and its initial carrier concentration is 5.0×10^{18} cm^{-3}. b) Normalized TA spectra (solid colored curves) which is extracted from (a) with the pump-probe delay ranging from 0.1 to 1 ps. Here, the Maxwell–Boltzmann fitting is applied to the high-energy tail of the normalized spectra (dashed black curves) starting from ≈0.5. c) HCs temperature kinetics extracted from the MB model at three selected carrier density (2.0, 5.0, and 8.5×10^{18} cm^{-3}). Dashed curves show our simplified TTM fitting. Note that to demonstrate the graph better, the cooling dynamics with the initial carrier concentration at 5.0 and 8.5×10^{18} cm^{-3} have 0.15 and 0.4 ps translation to the right, respectively.

© 2021 The Authors. Advanced Energy Materials published by Wiley-VCH GmbH

carrier-density-dependent bandgap renormalization (BGR) induced by many-body effect as well as Burstein–Moss effect (or band-filling, BF) induced by the Pauli exclusion principle that competes with each other in HOIPs.[25] As a result, the bandgap will shrink (by BGR) or widen (by BF), leading to red-shifts or blue-shifts respectively in the first picoseconds. An analysis between the two competing effects is given in the Note S3 (Supporting Information).

A normalized TA spectrum of the $MAPbBr_3$ film is shown in the Figure 1b at delay times from 0.1 to 1 ps. The spectrum shows an asymmetrically broadened tail due to the initial non-equilibrium HCs redistributing into a Fermi-Dirac distribution via electron–hole and carrier-carrier scattering.[26] The shrinkage of the tail corresponds to the cooling process of HCs mainly via electron-phonon coupling. The Fermi-Dirac distribution can be approximated to the Maxwell-Boltzmann distribution with carrier temperature T_c. The high-energy tail corresponds to higher T_c, and the carrier cooling rate is thus related to how fast this tail "relaxes". This tail is then fitted with the Maxwell-Boltzmann distribution,[8,21] from approximately half of the maximum value of the normalized TA spectra to a tail length of ≈0.27 eV in delay times ranging from 0.1 to 1 ps, as indicated by the dashed line in Figure 1b (normalization example in Figure S6 in the Supporting Information). Note that the extracted carrier temperature also depends on the choice of the region of interest.[27] However, our method shows robustness in the EPC calculation in spite of different reported fitting choices (details in Note S4, Supporting Information).

Figure 1c shows the electron temperature dynamics in $MAPbBr_3$ at three pump excitation powers corresponding to carrier densities; 2.0, 5.0, and 8.5×10^{18} cm^{-3}. The cooling process is dominated by electron-LO-phonon scattering mediated by polar Fröhlich interactions via LO phonon emission (details in Note S4, Supporting Information),[28] as well as cation vibrations, transmitting heat to the lattice. The HC temperature in $MAPbBr_3$ decays within 1.5 ps, in good agreement with the reported values in literature.[14]

2.2. Electron-Phonon Coupling Strength Analysis

To establish the average energy-transfer from the charge carriers to the lattice, we calculate the EPC coefficient using the HC temperature and cooling time. By obtaining the cooling dynamics through the analysis previously mentioned, the EPC strength can be derived via a two-temperature model (TTM) developed by Anisimov et al.–a technique that is widely used to analyze the EPC coefficient in ultrafast laser interactions with metals and semiconductors.[29] The temporal evolution of the electron and lattice temperatures can be described by the simultaneous differential equations[30,31]

$$C_e(T_e)\frac{\partial T_e}{\partial t} = -G_{el}(T_e - T_l) + P(t)$$
$$C_l(T_l)\frac{\partial T_l}{\partial t} = G_{el}(T_e - T_l) \quad (1)$$

where T_e and T_l are electron and lattice temperature, respectively, C_e and C_l are electron and lattice heat capacity, respectively, G_{el} is the EPC coefficient, $P(t)$ is a source term describing the energy injected by the femtosecond laser pulse within the first ≈100 fs. $C_l = C_v$ (300 K) − C_e (300 K) where C_v (300 K) is the total heat capacity of the sample at room temperature.[32] At low electron temperatures, the electron temperature can be approximated to have a linear dependence on electron heat capacity: $C_e = \gamma T_e$,[33] where γ is the electron heat capacity constant (Sommerfeld coefficient), and $\gamma = (\pi k_B)^2 g(E_F)/3$, determined by the density of state g at the Fermi level. Using the Sommerfeld free electron gas model, γ can be expressed with the free electron density n_e, $\gamma = (\pi k_B)^2 n_e/2E_F$. The free electron density is subsequently estimated by considering the HOIP crystal parameters. As shown in **Figure 2**a, HOIPs have pseudo-cubic ($MAPbI_3$) or cubic ($MAPbCl_3$, $MAPbBr_3$, $FAPbBr_3$) lattice systems at room temperature.[34] In cubic perovskite space group $pm\bar{3}m$, the unit cell contains 12 atoms.[35] In such case we simply assume that each Pb metal atom provides 2 free electrons, and we can obtain $n_e = 2/a^3 = 2\ N_A\ \rho/M$, where a is the lattice parameter, N_A is the Avogadro constant, ρ is the mass density, and M is the molar mass (see the Note S5 in the Supporting Information for details). The Sommerfeld coefficients are calculated for five different perovskites of form $APbX_3$ with the materials parameters reported in the literature presented in **Table 1**. The molar Sommerfeld coefficient varies for different materials such as superconductive perovskite $(K,Ba)BiO_3$ (3.5 mJ mol^{-1} K^{-2}),[36] semiconductor $FeGa_3$ (0.03 mJ mol^{-1} K^{-2}),[37] and Kondo semiconductor COs_2Al_{10} (7 mJ mol^{-1} K^{-2}),[38] and our calculated values are in the reasonable range. However, the volumetric coefficient is found to be smaller than that in metals such as Ag (62.8 J m^{-3} K^{-2}), Cu (71.0 J m^{-3} K^{-2}), and Au (62.9 J m^{-3} K^{-2}),[39] due to the lower free electron density. The calculated low value of γ is consistent to the low volumetric heat capacity of HOIPs.[40]

Equation (1) requires a description of the laser source term for which thermal and optical parameters such as coefficient of temperature resistance are needed. It describes how the energy density is absorbed, dependent on the laser penetration depth, the profile of the laser pulse, film thickness and the time-dependent absorbed fraction of the incident intensity happening on the ultrafast time scale. Due to the complexity of the mechanisms governing the initial heating of HOIPs, we simplify the TTM by neglecting the source term $P(t)$ and only consider the relaxation process which reveals the energy dissipation. The EPC can then be obtained by determining the electron temperature T_e at different delay times. T_e is obtained through the aforementioned Maxwell-Boltzmann distribution fit of the TA spectra at each time point. The decay of T_l is determined by the rate at which heat can diffuse away from the optically pumped region which typically happens on a relatively slow time scale (10–100s ps) compared to T_e. We thus assume that T_e is the main contribution to the relaxation signal in the first few ps.[30,32] Figure 1c demonstrates a good fit of our simplified TTM to the HCs cooling dynamics in $MAPbBr_3$ (black dashed curves). $MAPbI_3$ and $FAPbBr_3$ also show an excellent fitting in Figures S8a and S10 (Supporting Information). Note that when carrier density is even higher to 10^{19} cm^{-3}, the Auger reheating effect will further prolong the cooling process from ≈1 ps to tens of ps, leading to two sequential decays, as is in Figure S8b (Supporting Information).[12] We avoid this carrier-density region and only conduct experiments at moderate concentration

© 2021 The Authors. Advanced Energy Materials published by Wiley-VCH GmbH

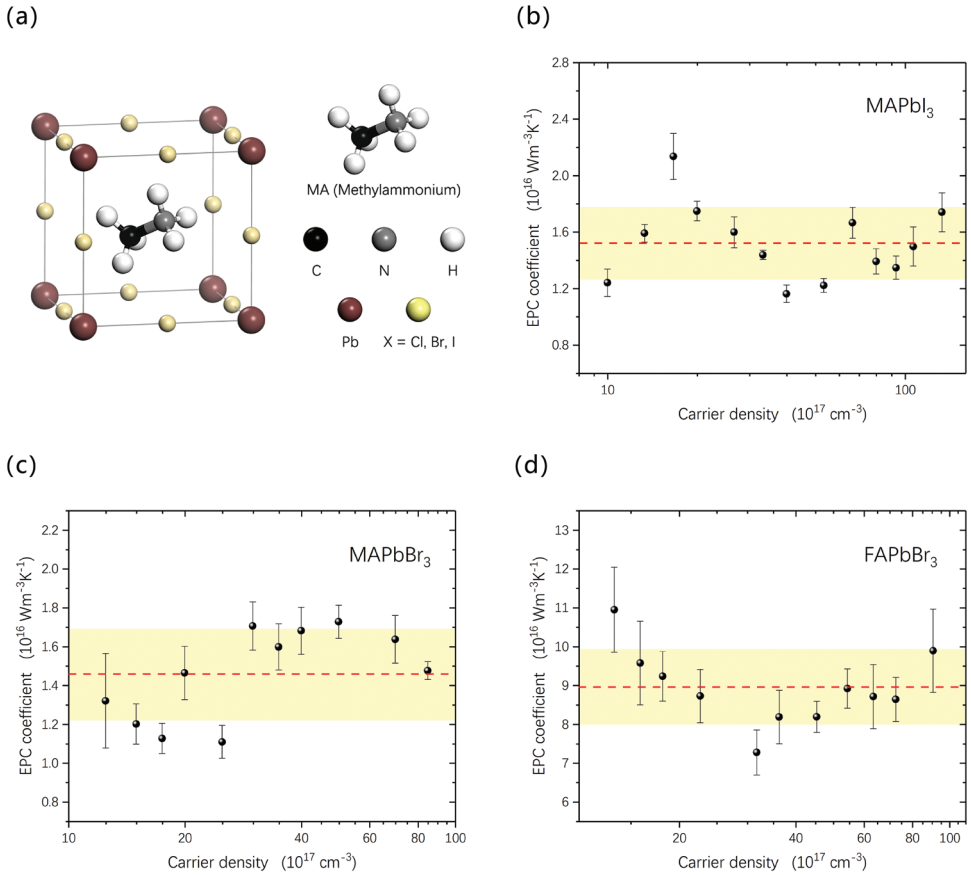

Figure 2. a) The lattice structure of MA-based HOIPs. Note that the unit cell of FA-based materials is basically the same with that of MA-based ones, where only the organic cation is different. b–d) The EPC strength in the $MAPbI_3$, $MAPbBr_3$, and $FAPbBr_3$ samples at different carrier densities. The red dashed line shows the average value while the yellow square demonstrates the standard deviation. Average values of EPC coefficients are b) 1.52 ± 0.27 (10^{16} W m^{-3} K^{-1}) in $MAPbI_3$, c) 1.46 ± 0.24 (10^{16} W m^{-3} K^{-1}) in $MAPbBr_3$, and d) 8.94 ± 0.98 (10^{16} W m^{-3} K^{-1}) in $FAPbBr_3$.

because our TTM only contains one decay. We find that as we vary the excitation power, the fitting is consistent and yields the values that are shown in Figure 2b–d. The average extracted values of EPC coefficient are 1.52 ± 0.27 (10^{16} W m^{-3} K^{-1}) in $MAPbI_3$, 1.46 ± 0.24 (10^{16} W m^{-3} K^{-1}) in $MAPbBr_3$ and 8.94 ± 0.98 (10^{16} W m^{-3} K^{-1}) in $FAPbBr_3$. For comparison, the G_{el} was obtained for the all-inorganic $CsPbI_3$ at ≈1.59 ± 0.18 (10^{16} W m^{-3} K^{-1}), however only three excitation power densities are presented due to the rapid degradation of the film (Figures S14 and S15, Supporting Information). The larger value of $FAPbBr_3$ is consistent with the observation of its shorter cooling time. The electron-phonon collision (scattering) time related to the G_{el} via $\tau_{e\text{-}ph} = C_e/G_{el}$ is evaluated at different carrier densities (Figure S16 and Note S6, Supporting Information), giving averaged values $\tau_{e\text{-}ph} \approx 0.40$ ps in $MAPbI_3$, ≈0.39 ps in $MAPbBr_3$, ≈0.15 ps in $FAPbBr_3$, and ≈0.44 ps in $CsPbI_3$. These values are comparable to traditional semiconductors such as GaAs ≈0.12 ps, Si ≈0.10 ps,[41] and CdTe ≈0.70 ps.[42] The values are also an order of magnitude lower than those found in superconductors such as $YBa_2Cu_3O_7$ ≈1.5 ps,[43] and $TlBa_2Ca_2Cu_3O_9$ ≈1.8 ps.[44] It is worth noting that the G_{el} values are an order of magnitude lower than reported values on metals such as nickel (≈8 × 10^{17} W m^{-3} K^{-1}),[31] copper (≈1 × 10^{17} W m^{-3} K^{-1}),[45] and platinum (≈2.5 × 10^{17} W m^{-3} K^{-1}).[45] This is a result of the small Sommerfeld coefficient and hence low heat capacity in HOIPs. The low EPC coefficient suggests weak energy transfer in the electron-lattice subsystem leading to inefficient heat dissipation, consistent with the accepted understanding of the slow cooling properties in HOIPs.[40]

Table 1. Lattice, electron and thermal parameters of $APbX_3$ at room temperature, where m_e is the electron effective mass and C_v is the total volumetric heat capacity.

System	$MAPbCl_3$	$MAPbBr_3$	$MAPbI_3$	$FAPbBr_3$	$CsPbI_3$
	cubic	cubic	pseudo-cubic	cubic	orthorhombic
Lattice constant (Å)	5.68[66]	5.90[66]	6.33[66]	5.99[35]	a = 10.46 b = 4.80 c = 17.77[67]
m_e (m_0)	0.36[68]	0.25[68]	0.33[68]	0.36[35]	0.22[69]
ρ (kg m^{-3})	3171[70]	3834[71]	4119[71]	3807[71]	–
C_v (MJ m^{-3} K^{-1})	1.62[70]	1.45[70]	1.28[70]	1.69[71]	1.00[a)]
γ (J m^{-3} K^{-2})	12.91	8.57	10.63	12.20	8.42
γ (mJ mol^{-1} K^{-2})	1.41	1.07	1.60	1.58	–

[a)]The C_v for $CsPbI_3$ is estimated to be 1 MJ m^{-3} K^{-1} based on the value for $CsPbBr_3$ (1.06 MJ m^{-3} K^{-1}).[71]

© 2021 The Authors. Advanced Energy Materials published by Wiley-VCH GmbH

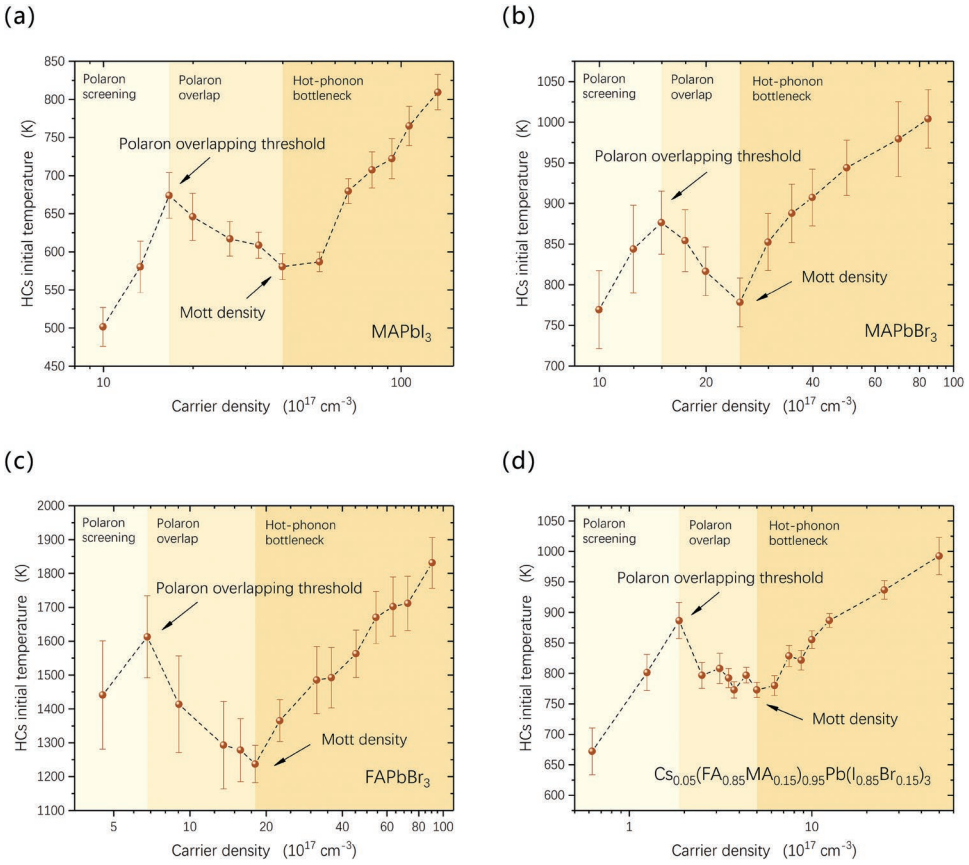

Figure 3. Carrier-density-dependent HCs initial temperature in the $MAPbI_3$, $MAPbBr_3$, $FAPbBr_3$, and $Cs_{0.05}(FA_{0.85}MA_{0.15})_{0.95}Pb(I_{0.85}Br_{0.15})_3$ respectively. The error bar at each brown dot comes from fitting deviation. The black dashed line links each dot together in the graph. The first peak in the initial temperature demonstrates the large polaron overlapping threshold, standing at a) 1.66×10^{18} cm^{-3} in $MAPbI_3$, b) 1.50×10^{18} cm^{-3} in $MAPbBr_3$, c) 0.68×10^{18} cm^{-3} in $FAPbBr_3$, and d) 0.19×10^{18} cm^{-3} in $Cs_{0.05}(FA_{0.85}MA_{0.15})_{0.95}Pb(I_{0.85}Br_{0.15})_3$. The second valley shows the critical Mott density in the nonmetal-metal transformation process at a) 3.99×10^{18} cm^{-3} in $MAPbI_3$, b) 2.50×10^{18} cm^{-3} in $MAPbBr_3$, c) 1.81×10^{18} cm^{-3} in $FAPbBr_3$, and d) 0.50×10^{18} cm^{-3} in $Cs_{0.05}(FA_{0.85}MA_{0.15})_{0.95}Pb(I_{0.85}Br_{0.15})_3$.

The EPC coefficient in the FA-based sample is distinctly larger than that in the two other MA-based perovskites, where the coefficients are almost identical mainly due to the higher initial HC temperature and faster rate of cooling measured, shown in Figures S8 and S10 (Supporting Information). With the same unit cell structure, the optical responses of these materials differ by the different organic cations.[8,28,46] The shorter cooling time in the FA-based perovskite is consistent with previous reports discussed by Zhu et al.,[17] showing that the organic cation can play a crucial role in the magnitude of the energy transfer between the electrons and the lattice. The polaron picture, despite being able to explain many of the extraordinary properties of HOIPs, leaves a question of how the polaron induced Coulomb screening interplays with the hot-phonon bottleneck and Auger reheating. In order to paint a more complete picture to not only characterize the microscopic energy transfer rate from carriers to electron-lattice subsystem but also comprehend the interplay between large polaron screening and hot-phonon bottleneck models, we have carried out a series of carrier-density-dependent HC experiments to investigate the dynamical screening-bottleneck competition in HOIPs.

Niesser et al. showed that polaron destabilization can induce a reduction of the initial carrier temperature with increasing carrier density.[16] We attempt to observe when the polarons completely overlap and when the hot-phonon bottleneck effect becomes dominant by expanding on the range of pumped carrier densities using transient absorption. Using the fitting derived in the above section, we fit the carrier temperature with the different time points and look at the initial carrier temperature with different pump densities. By taking initial carrier temperature at ≈0.1 ps approximately when the HCs have just been thermalized, we find a clear "S" shaped dependence of the initial carrier temperature on carrier density with $MAPbI_3$ shown in **Figure 3**a. The three shaded areas on the graph show that the initial temperature firstly increases (region I), followed by a temporary decrease down to a minimum value (region II), and finally ascends monotonically again (region III). Niesner et al., had reported the decrease of initial temperature with carrier concentration (region II). However, with further increase of carrier density (region III), we are able to see an increasing trend in initial temperatures, which agrees well with reports from Price et al.,[21] and Yang et al.[8] Our results show that at different carrier densities the initial carrier temperature variation is consistent with both the polaron screening and the hot-phonon bottleneck picture at different carrier densities, manifesting an "S" shape in Figure 3a. The study was carried out on $MAPbBr_3$, $FAPbBr_3$, and also a mixed cation $Cs_{0.05}(FA_{0.85}MA_{0.15})_{0.95}Pb(I_{0.85}Br_{0.15})_3$ to verify the generality of the results shown in Figure 3b–d. The initial carrier temperature

© 2021 The Authors. Advanced Energy Materials published by Wiley-VCH GmbH

is higher in the FA and mixed cation films despite the same excess energy pump used in all our experiments. We note that this may on the one hand be due to the emergence of additional relaxation pathways from larger density of sub-bandgap trapping states in $MAPbI_3$ resulting from the preparation methods.[15,47] On the other hand, this correlates well with the slower formation of polarons which protect the HC from quickly cooling in MA compared to cation perovskites.[48] Our study on the more novel mixed cation film hints that the polaron formation rate of the mixed cations perovskites lies between FA and MA rates. The result demonstrates that the stable mixed-perovskite has a higher initial carrier temperature than its MA- counterpart, promising for high voltage HC devices.

3. Discussions

3.1. Comparison to First-Principle Calculation of the EPC Values

We performed further analysis by first principles calculation of the EPC coefficient for the $MAPbBr_3$ and $FAPbBr_3$. Although a constant EPC coefficient is mainly investigated in experiments, there is growing evidence indicating that the applicability of the EPC strength may be limited to low laser intensities.[39] Here, the temperature-dependent electron heat capacity C_e, EPC coefficient G_{el} and electron-phonon scattering time $\tau_{e\text{-}ph}$ are numerically obtained as in refs. [49,50]. The description of numerical calculations based on the density functional theory (DFT) as well as formulas for the temperature-dependent C_e and G_{el} is provided in the Note S7 (Supporting Information). **Figure 4**a shows the calculated temperature-dependent electron heat capacity of the two materials. By taking into account the spin-orbit coupling effect, the density of states is found to be smaller, leading to a lower electron heat capacity for both MA and FA samples in comparison to the case presented in the Table 1. The EPC coefficient of $MAPbBr_3$ and $FAPbBr_3$ was calculated for the electronic temperatures of T_e = 1000 K and T_e = 1700 K, respectively, as is depicted in Figure 4b. The EPC coefficient shows a monotonic increase with the growth of electron temperature, which is consistent with the reported numerical results of metals such as Al, Ag, Cu, Au, and W.[39] The G_{el} of the MA material stands at 0.56 (10^{16} W m^{-3} K^{-1}) at 1000 K (the approximate initial HC temperature), which is much smaller than that of FA sample at 8.66 (10^{16} W m^{-3} K^{-1}) at 1700 K, in reasonable agreement with our experimental results. As is shown in Figure 4c, the electron-phonon collision time of MA and FA is calculated to be 0.56 ps at 1000 K and 0.14 ps at 1700 K, respectively, also agreeing well with the experimental value.

The experimental and theoretical EPC coefficient G_{el} presented for the MA- and FA-based perovskites show reasonable consistency. There are two findings we wish to address, firstly the difference in the values obtained between $FAPbBr_3$ and $MAPbBr_3$, and secondly the small variation in these values with different pump powers. The difference in EPC coefficients G_{el} of the FA- and the MA- films shows that the coupling strength between the charge carrier and the lattice varies with different organic cations. The scattering of charge carriers with phonons is treated within the polaron theory of Fröhlich, and the dimensionless Fröhlich coupling parameter $\alpha_{Fröhlich}$ characterizes the strength of the coupling between electrons and LO-phonons can be calculated by using materials parameters.[18,48] $\alpha_{Fröhlich}$ is shown to be larger in $FAPbBr_3$ (4.07),[20] compared to those of $MAPbBr_3$ (1.69), $MAPbI_3$ (1.71), and $CsPbI_3$ (1.35).[51] This trend is consistent with our EPC coefficient derived both experimentally and theoretically. We see that the larger LO phonon frequency and lower dielectric constant in the MA-based films effectively reduces its G_{el} value compared to that of $FAPbBr_3$. Our second observation, where G_{el} is almost constant with the increase of carrier pump density, suggests that the rate of energy transfer from the HC to the lattice remains more or less unchanged over a broad range. Since the total pumped energy increases linearly with the increase of pumped carrier density, the steady G_{el} value implies a monotonic growth in the HC cooling time. This is confirmed by our reported

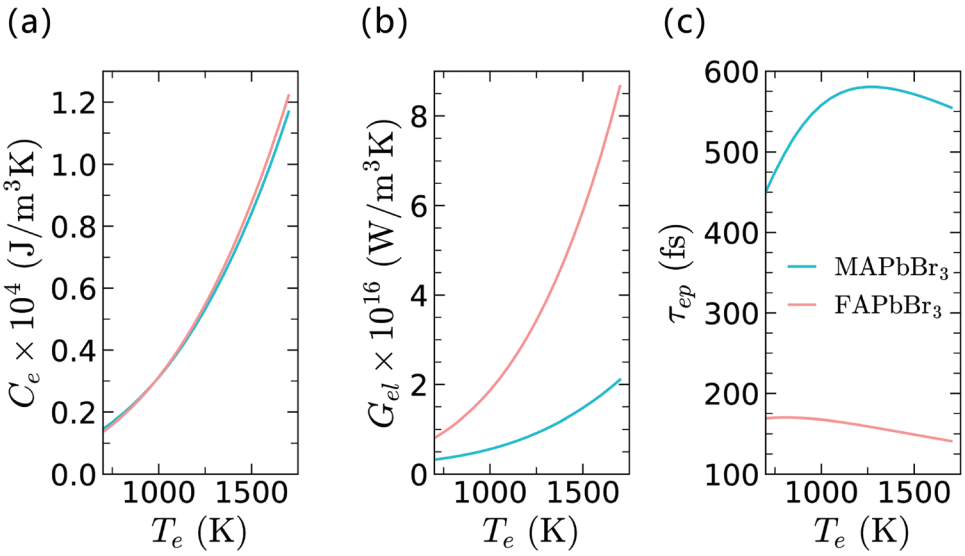

Figure 4. DFT calculations of electron-temperature-dependent a) electron heat capacity C_e, b) EPC coefficient G_{el}, and c) electron-phonon scattering time τ_{ep} for $MAPbBr_3$ (no symbols) and $FAPbBr_3$ (square symbols), respectively, with the temperature ranging from 700 to 1700 K.

© 2021 The Authors. Advanced Energy Materials published by Wiley-VCH GmbH

carrier-density-dependent linearly increasing carrier cooling time (from thermalization down to 400/600 K) in Figure S17 (Supporting Information). It is also consistent with results from Hopper et al., where the intra-band carrier cooling time linearly ascends from ≈0.1 to ≈0.8 ps with growing carrier density in various HOIPs via pump-push-probe measurement.[20,52]

3.2. The Anomalous Dependence of Electron Temperature with Carrier Density

For the second part of our study, we report an "S" shape in the initial temperature versus carrier density. In region I of Figure 3a, the gradual increase of carrier density causes a small increment in HC initial temperature while pumped with a constant excess energy to the band edge. In such low carrier densities, the phonon density should be sufficiently low that the hot-phonon bottleneck is insignificant to delay carrier cooling ($n < 10^{18}$ cm^{-3}).[16] However large polarons (covering ≈10 × unit cell dimensions) that form from HCs,[9] can result in efficient screening of the Coulomb potential in HOIPs. This polaron model has been shown to describe the large increases in dielectric constants in the high frequency THz range due to activation of PbX_3^- LO phonons.[18,53] The large dielectric constant helps to screen events involving Coulomb interaction such as carrier-phonon scattering.[54] Therefore, with the growth of carrier density, the average screening effect is expected to increase for the HCs, to which we ascribe the observed small rise in carrier initial energy (i.e., region I).

As the density of polarons increase, we see that the HCs initial temperature decreases with further pump density as indicated in region II of Figure 3a–d. This effect has previously been discussed and attributed to the destabilization effect induced by mutual repulsion of polarization clouds.[16,55] The polaron destabilization will undermine the large polaron "shield" against carrier-charged-defect and carrier-phonon interactions, resulting in the opposite trend of the carrier-density-related initial temperature. We point out that the peak between regions I and II in Figure 3a–d could be due to the onset of the large polaron overlap, at carrier densities 1.66×10^{18} cm^{-3} in $MAPbI_3$, 1.50×10^{18} cm^{-3} in $MAPbBr_3$, 0.68×10^{18} cm^{-3} in $FAPbBr_3$, and 0.19×10^{18} cm^{-3} in $Cs_{0.05}(FA_{0.85}MA_{0.15})_{0.95}Pb(I_{0.85}Br_{0.15})_3$. According to Frost's model, if "overlap" is simply defined as when polarons "touch", the maximum polaron radius r_P can be estimated via the critical overlapping density n_o[22]

$$\frac{1}{n_o} = 2\left(2r_P^{\text{Frost}}\right)^3 \tag{2}$$

where a factor of 2 is included for capturing both hole and electron polarons. The estimated polaron radius using Frost's model is shown in Table S2 (Supporting Information) and in reasonable agreement with literature reported values. This polaron radius spans over several unit cells, consistent with the large polaron picture.[9] Notably, the polaron radii of the FA-based and the mixed cation perovskite are significantly larger. Such difference may be attributed to comparatively weaker polarization in FA samples judging from Zhu et al. TR-OKE plots, where the signal of organic cations' liquid-like re-orientational motion which results in large polaron formation and thus the Coulomb screening in MA cation films is stronger than in the FA.[17]

With further growth in carrier density, the increasing trend in initial temperature once again dominates via the hot-phonon bottleneck effect as depicted in region III of Figure 3a–d. The minimal value between regions II and III here signals a change in the predominant effect which retards the HC cooling, from dynamical screening being destabilized and the hot-phonon bottleneck. In the polaron generation model, following photon excitation, the charge carriers will form large polarons covering multiple unit cells. Suppose that the pumped carriers become densely packed such that there is significant interaction immediately after photo-generation. A transition in the state of the material in this time scale can occur described as the phenomenological critical Mott density.[56] The Mott density quantitatively characterizes the transition from an insulating exciton gas at lower carrier concentrations to a metal-like state of an electron-hole plasma at higher concentrations during the very initial generation of the carriers.[57] The three carrier density regimes are illustrated in a schematic in **Figure 5**. Taking the minimum point in our plots in Figure 3a–d, the Mott densities extracted are: 3.99×10^{18} cm^{-3} in $MAPbI_3$, 2.50×10^{18} cm^{-3} in $MAPbBr_3$, 1.81×10^{18} cm^{-3} in $FAPbBr_3$, and 0.50×10^{18} cm^{-3} in $Cs_{0.05}(FA_{0.85}MA_{0.15})_{0.95}Pb(I_{0.85}Br_{0.15})_3$). Using these values, we attempt to estimate the Bohr radius and exciton binding energy by applying Edward's model and Haug–Schmitt–Rink's (HSR) model that describes the nonmetal-metal transition with universal applications detailed in Note S8 (Supporting Information). As summarized in Table S2 (Supporting Information), our estimated values of the Bohr radii for $MAPbI_3$: 1.64 nm, $MAPbBr_3$: 1.92 nm, and $FAPbBr_3$: 2.13 nm show reasonable consistency with reported results.

The smaller Mott density found in the FA-based and mixed sample results in a larger calculated Bohr radius. As for the exciton binding energy, values reported in the literature cover a broad range from 2 to 55 meV in $MAPbI_3$,[58–60] and from 40.3 to 150 meV in $MAPbBr_3$,[58,59,61,62] with more recent reports suggesting lower values due to more sophisticated calculation models and higher-quality samples.[63] Our exciton binding energy of $MAPbI_3$: 16.9 meV and $MAPbBr_3$: 36 meV is in agreement with more recently reported results. We also estimate the exciton binding energy in $FAPbBr_3$: 9.3 meV and the Bohr radius of $Cs_{0.05}(FA_{0.85}MA_{0.15})_{0.95}Pb(I_{0.85}Br_{0.15})_3$: 3.28 nm (details in Table S2, Supporting Information), which has had fewer reports. In comparison to the density-dependent time-resolved PL spectroscopy which was previously used to study the Mott transition,[64] we show that by analyzing the HC initial temperatures, not only the transition process but the polaron size, Bohr radii and exciton binding energy can also be simultaneously determined.

It is clear that the major applications of HCs strongly depend upon prolonging cooling lifetimes that can benefit the efficient HC extraction in high-efficiency solar cells development. In conventional semiconductors, it still remains a challenge to materialize slow HC cooling even in strongly quantum-confined system due to the emergence of additional relaxation pathways including Auger energy transfer from the hot electrons to the dense hole states, atomic fluctuations, and defect trapping offsetting the enhanced phonon bottleneck effect.[9] However, in weakly quantum-confined HOIP NCs, Sum et al.

© 2021 The Authors. Advanced Energy Materials published by Wiley-VCH GmbH

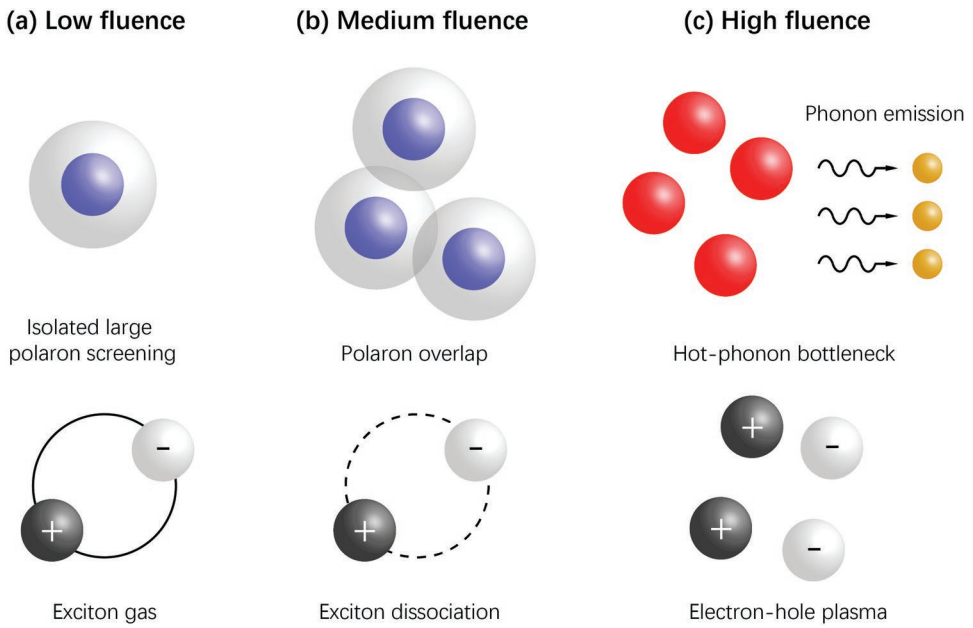

Figure 5. Dominant cooling mechanism and microscopic physical process involved at different carrier density. a) Isolated large polaron screening effect at low carrier concentration; b) large polaron destabilization induced by overlapping effect at medium density, where the Mott nonmetal-metal transition from insulating exciton gas to the metal-like electron–hole plasma takes place; c) hot-phonon bottleneck effect pumped at high fluence, where materials show metal-like properties induced by electron-hole plasma.

reported that the absent hole manifold can retain the intrinsic phonon-bottleneck effect, demonstrating unparalleled superiority compared to the bulk counterparts and traditional semiconductors.[14] Much slower cooling (up to ≈30 ps) can be achieved in colloidal $MAPbBr_3$ NCs at above ≈10^{18} cm^{-3} due to enhanced Auger reheating effect, while the abovementioned additional competing relaxation pathways are shown to be effectively suppressed. Meanwhile, the efficient acoustic-optical phonon up-conversion can also retard the rapid cooling by reheating carriers via recycled thermal energy. Yang et al. based their theory in $FAPbI_3$ bulk film on the formerly reported classification of low-energy optical-like "hybrid phonon" in a thermally insulating 2D multiferroic perovskite-like system $(C_6H_5CH_2CH_2NH_3)_2CuCl_4$.[65] They discovered that the better overlapping phonon branches by organic cations, stronger acoustic phonon localization and lower thermal conductivity can help enhance the up-transition of low-energy phonon modes, thus prolonging the cooling to even over 100 ps.[15] We base our theory on HOIP bulk systems; nevertheless, given the ultra-long HC cooling in the lower dimensional quantum-confined HOIP structures, future efforts are needed for deciphering the competitive effects among the aforementioned carrier-density-dependent enhanced mechanisms.

In conclusion, we report a method of extracting EPC coefficients of perovskite thin films directly by using transient absorption spectroscopy. HC cooling dynamics of HOIPs are analyzed by fitting with a simplified TTM to determine the EPC coefficients. The values are reported for $MAPbI_3$, $FAPbBr_3$, and $MAPbBr_3$, and found to correlate well with their respective HC cooling rates. In addition, DFT calculations are performed in order to theoretically obtain the EPC coefficients, which are consistent with our experimental values. Through analysis of the carrier temperatures versus pump fluence, we report an interesting "S" shape relationship where we identify the onset of large polaron overlap and also determine the Mott density. Our result provides a clear comparison between some of the past contradictory experimental results, putting competitive HC cooling mechanisms in HOIPs into perspective. The comprehensive understanding of the cooling mechanisms will lay the foundation for effective exploitation of the slowed-cooling properties, helping to accelerate the development of prospective high-performance photovoltaic devices.

4. Experimental Section

Details of sample fabrication methods are provided in note S9 of the Supporting Information. Absorption of the thin $MAPbBr_3$, $FAPbBr_3$, and $MAPbI_3$ was measured by UV–vis spectroscopy using a PerkinElmer LAMBDA 900. Transient absorption measurements were carried out using a home-built pump probe setup. Time integrated PL was performed with excitation with a 405 nm diode laser, ready to be collected and analyzed with a CCD integrated spectrometer. See Note S10 of Supporting Information for details.

Supporting Information

Supporting Information is available from the Wiley Online Library or from the author.

Acknowledgements

This work is partially supported by the Hong Kong Research Grants Council (project number AoE/P-02/12) and William Mong Institute

© 2021 The Authors. Advanced Energy Materials published by Wiley-VCH GmbH

of Nano Science and Technology (project number WMINST19/SC04). The authors also acknowledge European Union through the European Regional Development Fund – the Competitiveness and Cohesion Operational Programme (Grant No. KK.01.1.1.06) and "Center of Excellence for Advanced Materials and Sensing Devices" (Grant No. KK.01.1.1.01.0001), project PZS-2019-02-2068 financed by the "Research Cooperability" Program of the Croatian Science Foundation funded by the European Union from the European Social Fund under the Operational Programme Efficient Human Resources 2014–2020, and Croatian Science Foundation Grant No. UIP-2019-04-6869. Special thanks go to K. F. Yeung for the technical support.

Conflict of Interest

The authors declare no conflict of interest.

Author Contributions

C.C.S.C. and K.F. contributed equally to this work. C.C.S.C., K.F., and K.S.W. conceived the idea for the manuscript and designed the experiments. C.C.S.C. conducted the transient absorption measurement. H.W., K.Y., Z.H., J.X., and W.C.H.C. provided samples and materials characterization. D.N. and I.L. conducted DFT based calculations. C.C.S.C., K.F., and K.S.W. analyzed the experimental data and wrote the manuscript. All authors discussed the results and commented on the manuscript at all stages. K.S.W. led the project.

Data Availability Statement

Data available on request from the authors.

Keywords

electron-phonon coupling, hot-phonon bottleneck effect, large-polaron screening effect, lead halide perovskites, Mott density

Received: September 27, 2020
Revised: January 1, 2021
Published online: January 27, 2021

[1] M. M. Lee, J. Teuscher, T. Miyasaka, T. N. Murakami, H. J. Snaith, *Science* **2012**, *338*, 643.
[2] P. Qin, S. Tanaka, S. Ito, N. Tetreault, K. Manabe, H. Nishino, M. K. Nazeeruddin, M. Grätzel, *Nat. Commun.* **2014**, *5*, 3834.
[3] W. S. Yang, B. W. Park, E. H. Jung, N. J. Jeon, Y. C. Kim, D. U. Lee, S. S. Shin, J. Seo, E. K. Kim, J. H. Noh, S. Il Seok, *Science* **2017**, *356*, 1376.
[4] J. Xie, P. Hang, H. Wang, S. Zhao, G. Li, Y. Fang, F. Liu, X. Guo, H. Zhu, X. Lu, X. Yu, C. C. S. Chan, K. S. Wong, D. Yang, J. Xu, K. Yan, *Adv. Mater.* **2019**, *31*, 1902543.
[5] G. Xing, N. Mathews, S. Sun, S. S. Lim, Y. M. Lam, M. Graẗzel, S. Mhaisalkar, T. C. Sum, *Science* **2013**, *342*, 344.
[6] H. Zhu, Y. Fu, F. Meng, X. Wu, Z. Gong, Q. Ding, M. V. Gustafsson, M. T. Trinh, S. Jin, X. Y. Zhu, *Nat. Mater.* **2015**, *14*, 636.
[7] H. Utzat, W. Sun, A. E. K. Kaplan, F. Krieg, M. Ginterseder, B. Spokoyny, N. D. Klein, K. E. Shulenberger, C. F. Perkinson, M. V. Kovalenko, M. G. Bawendi, *Science* **2019**, *363*, 1068.
[8] Y. Yang, D. P. Ostrowski, R. M. France, K. Zhu, J. Van De Lagemaat, J. M. Luther, M. C. Beard, *Nat. Photonics* **2016**, *10*, 53.
[9] M. Li, J. Fu, Q. Xu, T. C. Sum, *Adv. Mater.* **2018**, *31*, 1802486.
[10] R. T. Ross, A. J. Nozik, *J. Appl. Phys.* **1982**, *53*, 3813.
[11] S. Kahmann, M. A. Loi, *J. Mater. Chem. C* **2019**, *7*, 2471.
[12] J. Fu, Q. Xu, G. Han, B. Wu, C. H. A. Huan, M. L. Leek, T. C. Sum, *Nat. Commun.* **2017**, *8*, 1300.
[13] M. Achermann, A. P. Bartko, J. A. Hollingsworth, V. I. Klimov, *Nat. Phys.* **2006**, *2*, 557.
[14] M. Li, S. Bhaumik, T. W. Goh, M. S. Kumar, N. Yantara, M. Grätzel, S. Mhaisalkar, N. Mathews, T. C. Sum, *Nat. Commun.* **2017**, *8*, 14350.
[15] J. Yang, X. Wen, H. Xia, R. Sheng, Q. Ma, J. Kim, P. Tapping, T. Harada, T. W. Kee, F. Huang, Y.-B. Cheng, M. Green, A. Ho-Baillie, S. Huang, S. Shrestha, R. Patterson, G. Conibeer, *Nat. Commun.* **2017**, *8*, 14120.
[16] D. Niesner, H. Zhu, K. Miyata, P. P. Joshi, T. J. S. Evans, B. J. Kudisch, M. T. Trinh, M. Marks, X. Y. Zhu, *J. Am. Chem. Soc.* **2016**, *138*, 15717.
[17] H. Zhu, K. Miyata, Y. Fu, J. Wang, P. P. Joshi, D. Niesner, K. W. Williams, S. Jin, X. Y. Zhu, *Science* **2016**, *353*, 1409.
[18] K. Miyata, D. Meggiolaro, M. T. Trinh, P. P. Joshi, E. Mosconi, S. C. Jones, F. De Angelis, X.-Y. Zhu, *Sci. Adv.* **2017**, *3*, 1701217.
[19] T. J. S. Evans, K. Miyata, P. P. Joshi, S. Maehrlein, F. Liu, X.-Y. Zhu, *J. Phys. Chem. C* **2018**, *122*, 13724.
[20] T. R. Hopper, A. Gorodetsky, J. M. Frost, C. Müller, R. Lovrincic, A. A. Bakulin, *ACS Energy Lett.* **2018**, *3*, 2199.
[21] M. B. Price, J. Butkus, T. C. Jellicoe, A. Sadhanala, A. Briane, J. E. Halpert, K. Broch, J. M. Hodgkiss, R. H. Friend, F. Deschler, *Nat. Commun.* **2015**, *6*, 8420.
[22] J. M. Frost, L. D. Whalley, A. Walsh, *ACS Energy Lett.* **2017**, *2*, 2647.
[23] S. V. Kilina, D. S. Kilin, O. V. Prezhdo, *ACS Nano* **2009**, *3*, 93.
[24] A. M. A. Leguy, P. Azarhoosh, M. I. Alonso, M. Campoy-Quiles, O. J. Weber, J. Yao, D. Bryant, M. T. Weller, J. Nelson, A. Walsh, M. Van Schilfgaarde, P. R. F. Barnes, *Nanoscale* **2016**, *8*, 6317.
[25] M. Feneberg, S. Osterburg, K. Lange, C. Lidig, B. Garke, R. Goldhahn, E. Richter, C. Netzel, M. D. Neumann, N. Esser, S. Fritze, H. Witte, J. Bläsing, A. Dadgar, A. Krost, *Phys. Rev. B* **2014**, *90*, 075203.
[26] D. W. Snoke, W. W. R̈hle, Y. C. Lu, E. Bauser, *Phys. Rev. B* **1992**, *45*, 10979.
[27] J. W. M. Lim, D. Giovanni, M. Righetto, M. Feng, S. G. Mhaisalkar, N. Mathews, T. C. Sum, *J. Phys. Chem. Lett.* **2020**, *11*, 2743.
[28] A. D. Wright, C. Verdi, R. L. Milot, G. E. Eperon, M. A. Pérez-Osorio, H. J. Snaith, F. Giustino, M. B. Johnston, L. M. Herz, *Nat. Commun.* **2016**, *7*, 11755.
[29] S. Anisimov, B. Kapeliovich, T. Perel'Man, *Sov. J. Exp. Theor. Phys.* **1974**, *39*, 776.
[30] S. D. Brorson, A. Kazeroonian, J. S. Moodera, D. W. Face, T. K. Cheng, E. P. Ippen, M. S. Dresselhaus, G. Dresselhaus, *Phys. Rev. Lett.* **1990**, *64*, 2172.
[31] E. Beaurepaire, J. C. Merle, A. Daunois, J. Y. Bigot, *Phys. Rev. Lett.* **1996**, *76*, 4250.
[32] Z. Luo, T. Shu, Z. Chen, T. Jiang, H. Wu, T. Lai, *Semicond. Sci. Technol.* **2019**, *34*, 105011.
[33] M. D. Watson, T. K. Kim, A. A. Haghighirad, N. R. Davies, A. McCollam, A. Narayanan, S. F. Blake, Y. L. Chen, S. Ghannadzadeh, A. J. Schofield, M. Hoesch, C. Meingast, T. Wolf, A. I. Coldea, *Phys. Rev. B* **2015**, *91*, 155106.
[34] G. Giorgi, J.-I. Fujisawa, H. Segawa, K. Yamashita, *J. Phys. Chem. Lett.* **2013**, *4*, 4213.
[35] M. Roknuzzaman, J. A. Alarco, H. Wang, A. Du, T. Tesfamichael, K. (Ken) Ostrikov, *Comput. Mater. Sci.* **2019**, *169*, 109118.
[36] T. Klein, C. Marcenat, F. Bouquet, A. Junod, S. Blanchard, J. Marcus, *Phys. C* **2004**, *408–410*, 731.
[37] B. Kotur, V. Babizhetskyy, E. Bauer, F. Kneidinger, A. Danner, L. Leber, H. Michor, *Mater. Sci.* **2013**, *49*, 211.

© 2021 The Authors. Advanced Energy Materials published by Wiley-VCH GmbH

[38] J. Kawabata, T. Takabatake, K. Umeo, Y. Muro, *Phys. Rev. B* **2014**, *89*, 094404.
[39] Z. Lin, L. V. Zhigilei, V. Celli, *Phys. Rev. B* **2008**, *77*, 075133.
[40] T. Haeger, M. Wilmes, R. Heiderhoff, T. Riedl, *J. Phys. Chem. Lett.* **2019**, *10*, 3019.
[41] I. B. Bogatyrev, D. Grojo, P. Delaporte, S. Leyder, M. Sentis, W. Marine, T. E. Itina, *J. Appl. Phys.* **2011**, *110*, 103106.
[42] M. Betz, G. Göger, A. Leitenstorfer, K. Ortner, C. R. Becker, G. Böhm, A. Laubereau, *Phys. Rev. B* **1999**, *60*, R11265.
[43] M. Johnson, *Appl. Phys. Lett.* **1991**, *59*, 1371.
[44] A. D. Semenov, R. S. Nebosis, M. A. Heusinger, K. F. Renk, *Phys. C* **1994**, *235*, 1971.
[45] J. Hohlfeld, S. S. Wellershoff, J. Güdde, U. Conrad, V. Jähnke, E. Matthias, *Chem. Phys.* **2000**, *251*, 237.
[46] H. Kawai, G. Giorgi, A. Marini, K. Yamashita, *Nano Lett.* **2015**, *15*, 3103.
[47] Z. Zhang, J. Yang, X. Wen, L. Yuan, S. Shrestha, J. A. Stride, G. J. Conibeer, R. J. Patterson, S. Huang, *J. Phys. Chem. C* **2015**, *119*, 24149.
[48] K. Miyata, T. L. Atallah, X.-Y. Zhu, *Sci. Adv.* **2017**, *3*, 1701469.
[49] D. Novko, J. C. Tremblay, M. Alducin, J. I. Juaristi, *Phys. Rev. Lett.* **2019**, *122*, 016806.
[50] D. Novko, F. Caruso, C. Draxl, E. Cappelluti, *Phys. Rev. Lett.* **2020**, *124*, 077001.
[51] J. M. Frost, *Phys. Rev. B* **2017**, *96*, 195202.
[52] T. R. Hopper, A. Gorodetsky, A. Jeong, F. Krieg, M. I. Bodnarchuk, M. Maimaris, M. Chaplain, T. J. Macdonald, X. Huang, R. Lovrincic, M. V. Kovalenko, A. A. Bakulin, *Nano Lett.* **2020**, *20*, 2271.
[53] I. Anusca, S. Balčiūnas, P. Gemeiner, Š. Svirskas, M. Sanlialp, G. Lackner, C. Fettkenhauer, J. Belovickis, V. Samulionis, M. Ivanov, B. Dkhil, J. Banys, V. V. Shvartsman, D. C. Lupascu, *Adv. Energy Mater.* **2017**, *7*, 1700600.
[54] X.-Y. Zhu, V. Podzorov, *J. Phys. Chem. Lett.* **2015**, *6*, 4758.
[55] D. Emin, *Polarons*, Cambridge University Press, Cambridge **2010**.
[56] P. P. Joshi, S. F. Maehrlein, X. Zhu, *Adv. Mater.* **2019**, *31*, 1803054.
[57] C. L. Davies, M. R. Filip, J. B. Patel, T. W. Crothers, C. Verdi, A. D. Wright, R. L. Milot, F. Giustino, M. B. Johnston, L. M. Herz, *Nat. Commun.* **2018**, *9*, 293.
[58] Y. Yang, M. Yang, Z. Li, R. Crisp, K. Zhu, M. C. Beard, *J. Phys. Chem. Lett.* **2015**, *6*, 4688.
[59] V. D'Innocenzo, G. Grancini, M. J. P. Alcocer, A. R. S. Kandada, S. D. Stranks, M. M. Lee, G. Lanzani, H. J. Snaith, A. Petrozza, *Nat. Commun.* **2014**, *5*, 3586.
[60] S. Sun, T. Salim, N. Mathews, M. Duchamp, C. Boothroyd, G. Xing, T. C. Sum, Y. M. Lam, *Energy Environ. Sci.* **2014**, *7*, 399.
[61] I. B. Koutselas, L. Ducasse, G. C. Papavassiliou, *J. Phys.: Condens. Matter* **1996**, *8*, 1217.
[62] Y. Yang, Y. Yan, M. Yang, S. Choi, K. Zhu, J. M. Luther, M. C. Beard, *Nat. Commun.* **2015**, *6*, 7961.
[63] A. Miyata, A. Mitioglu, P. Plochocka, O. Portugall, J. T. W. Wang, S. D. Stranks, H. J. Snaith, R. J. Nicholas, *Nat. Phys.* **2015**, *11*, 582.
[64] L. Kappei, J. Szczytko, F. Morier-Genoud, B. Deveaud, *Phys. Rev. Lett.* **2005**, *94*, 147403.
[65] A. Caretta, M. C. Donker, D. W. Perdok, D. Abbaszadeh, A. O. Polyakov, R. W. A. Havenith, T. T. M. Palstra, P. H. M. Van Loosdrecht, *Phys. Rev. B* **2015**, *91*, 1.
[66] A. Poglitsch, D. Weber, *J. Chem. Phys.* **1987**, *87*, 6373.
[67] R. J. Sutton, M. R. Filip, A. A. Haghighirad, N. Sakai, B. Wenger, F. Giustino, H. J. Snaith, *ACS Energy Lett.* **2018**, *3*, 1787.
[68] Y. H. Chang, C. H. Park, K. Matsuishi, *J. Korean Phys. Soc.* **2004**, *44*, 638.
[69] M. Afsari, A. Boochani, M. Hantezadeh, *Optik* **2016**, *127*, 11433.
[70] O. Knop, R. E. Wasylishen, M. A. White, T. S. Cameron, M. J. M. Van Oort, *Can. J. Chem.* **1990**, *68*, 412.
[71] G. A. Elbaz, W.-L. L. Ong, E. A. Doud, P. Kim, D. W. Paley, X. Roy, J. A. Malen, *Nano Lett.* **2017**, *17*, 5734.

© 2021 The Authors. Advanced Energy Materials published by Wiley-VCH GmbH